Available online at www.sciencedirect.com

SciVerse ScienceDirect

Acta Materialia 60 (2012) 702–715

Acta MATERIALIA

www.elsevier.com/locate/actamat

Anisotropic stress–strain response and microstructure evolution of textured α-uranium

Marko Knezevic [a,*], Laurent Capolungo [b], Carlos N. Tomé [a], Ricardo A. Lebensohn [a], David J. Alexander [a], Bogdan Mihaila [a], Rodney J. McCabe [a]

[a] Materials Science and Technology Division, Los Alamos National Laboratory, Los Alamos, NM 87545, USA
[b] George Woodruff School of Mechanical Engineering, Georgia Institute of Technology, UMI 2958 Georgia Tech – CNRS, 57070 Metz, France

Received 8 September 2011; received in revised form 20 October 2011; accepted 21 October 2011

Abstract

The deformation behavior of wrought α-uranium is studied using electron backscattered diffraction and crystal plasticity modeling. We report stress–strain response and texture evolution for 12 different cases corresponding to tension and compression tests performed on three different initial textures: straight-rolled, clock-rolled and swaged α-uranium. It is seen that the response of α-uranium is highly anisotropic owing to its low-symmetry orthorhombic crystal structure and limited number of slip/twin systems. For modeling this complex system, we adapt a multiscale dislocation-based hardening law developed earlier for hexagonal metals and implement it within a viscoplastic self-consistent homogenization scheme. This hardening law performs well in capturing the anisotropic strain hardening and the texture evolution in all studied samples. Comparisons of simulations and experiments allow us to infer basic information concerning the various slip and twin mechanisms, their interactions, and their role on strain hardening and texture evolution in α-uranium.

Keywords: Uranium; Constitutive modeling; Texture; Twinning; EBSD

1. Introduction

Polycrystal plasticity models have been evolving in order to model increasingly complex deformation behaviors. The degree of sophistication necessary to accurately model a material generally scales with the number and types of deformation modes active in a material. Metals with multiple active slip modes are more complicated than metals with a single slip mode, and metals that deform by twinning are considerably more difficult to model than metals that only deform by dislocation slip. Uranium, an important metal for nuclear fuels and defense applications, is a challenging material to accurately model because it exhibits four different slip modes and at least three different deformation twinning modes. For this reason, uranium presents a challenging test to the validity of deformation models.

At room temperature uranium has a base-centered orthorhombic crystal structure (α-uranium) with lattice parameters $a = 0.2852$ nm, $b = 0.5865$ nm and $c = 0.4945$ nm [1]. Operation of multiple slip and twinning modes with low multiplicity and widely different activation stresses are generally necessary to accommodate plastic strain. Consequently, the plastic response is markedly anisotropic and hardening depends strongly on texture and on the interactions between these slip and twin modes. The only feasible approach for developing a constitutive law for uranium is to base it on crystal plasticity rather than on a continuum approach. To date, only a single study [2] using a limited experimental data set has been conducted using crystal plasticity to model uranium.

Several studies in the 1950s through the early 1970s examined the deformation mechanisms active in single-crystal and large-grained uranium [1,3–6], and there have

* Corresponding author. Tel.: +1 505 665 7587; fax: +1 505 667 8021.
E-mail address: knezevic@lanl.gov (M. Knezevic).

1359-6454/$36.00
doi:10.1016/j.actamat.2011.10.041

been some limited efforts to model texture evolution during processing of uranium [7,8]. More recently, the utilization of new experimental characterization and modeling techniques has thrown new light on the basic deformation behavior of uranium [2,9,10]. Up to 350 °C, the easiest slip mode in α-uranium is (0 1 0)[1 0 0] [5,11]. The (0 0 1)[1 0 0] slip mode operates mainly in the form of cross-slip up to 350 °C, when it becomes the primary slip mode [5,11], with each of the above slip modes comprising only a single slip system. The $1/2\{0\,2\,1\}\langle 1\,\bar{1}\,2\rangle$ slip mode is also found to be an active deformation mode, with two slip systems. However, its activation requires a larger driving force than the primary (0 1 0)[1 0 0] slip mode [5]. The $1/2\{1\,\bar{1}\,2\}\langle 0\,2\,1\rangle$ slip mode offers the additional degree of freedom necessary to accommodate plastic strain in the [0 0 1] direction and, thus, to accommodate an arbitrary plastic strain.

In addition to slip, twinning plays a significant role in plastic deformation of α-uranium. The most prominent deformation twin in α-uranium is the $\{1\,3\,0\}\langle 3\,\bar{1}\,0\rangle$ twin mode [1,3,5]. The $\{1\,7\,2\}\langle 3\,\bar{1}\,2\rangle$ twin mode and its reciprocal twin $\{1\,1\,2\}\langle 3\,\bar{7}\,2\rangle$ are also frequently observed in wrought uranium [1,3,5]. The $\{1\,3\,0\}\langle 3\,\bar{1}\,0\rangle$ and $\{1\,7\,2\}\langle 3\,\bar{1}\,2\rangle$ twins have twinning shears of 0.299 and 0.227, respectively, and reorient the crystal lattice by 69.3° about [0 0 1] and 92.6° about $\langle\overline{1}070\rangle$, respectively. Depending on the twin mode activity (i.e. the nucleation and the propagation), the crystal lattice reorientation of the two twinning modes is expected to have a significant influence on crystallographic texture evolution and strain hardening.

Deformation twinning contributes to strain hardening in several ways. The propagation of the twin interface into a domain containing dislocations can lead to: (1) transmutation of dislocations from glissile to sessile, and (2) dissociation of dislocations upon meeting the twin interface [12]. In addition, it has been suggested that a Hall–Petch-type effect could arise from grain subdivision associated with twinning [13–15]. The source of the Hall–Petch effect is traditionally attributed to the formation of pile-ups or to strain gradients at interfaces. Finally, twinning also leads to crystal lattice reorientation into either a harder or a softer orientation (texture hardening or softening). In this case, the activation of slip (referred to as secondary slip) within twinned volumes can become particularly relevant for hardening. For cases when twins grow at a fast rate and readily consume entire grains, the Hall–Petch-like hardening effect is not expected to be significant, and the major contribution to strain hardening resulting from twinning will be through texture hardening [16].

In the present paper, we have conducted a number of experiments and numerical simulations in an effort to explain and develop new physical insights into the phenomena described above. In particular, we have analyzed and quantified the effects of starting texture on microstructure evolution and mechanical response of α-uranium. A large body of experimental data has been collected using standard mechanical testing and electron backscattered diffraction (EBSD) on three classes of wrought α-uranium samples having similar grain sizes but different textures. The samples were classified according to their processing history as clock-rolled (CR), straight-rolled (SR) and swaged (SW). Some of the results presented regarding the CR samples were published in previous papers [2,9]. However, for the sake of completeness of the present study, we include some of these experimental results here. In recent work [2] on the polycrystalline modeling of CR α-uranium it was shown that a multiscale constitutive model developed initially for hexagonal polycrystalline metals can be adapted for modeling the anisotropic stress–strain response and texture evolution of α-uranium. Here we use the same multiscale modeling approach as in Refs. [2,17], apply it to a comprehensive set of experimental data and subsequently interpret the model predictions in terms of the physical influence of the various deformation mechanisms and their interactions on the mechanical response, the strain-hardening rates and the texture evolution in α-uranium.

2. Materials and experimental methods

The starting materials were vacuum induction cast uranium ingots that were further processed by various series of thermomechanical steps in order to introduce three different microstructures and textures in the samples relevant to the present study. For all materials, the ingots were first upset forged and then hot rolled at 640 °C in multiple passes to a thickness of around 32 mm followed by annealing at 480 °C for 2 h. The materials were then warm rolled at 330 °C in multiple passes to a thickness of 15 mm with the CR material being rotated in multiples of 45° between rolling passes, and the SR and SW material always having the same rolling direction. A 15 mm diameter rod was machined from part of the SR material to be swaged in the final working operation. The SW material was swaged to a final diameter of 9.6 mm at room temperature in a series of three swaging steps. The CR and SR materials were warm rolled to a final thickness of about 8 mm. Finally, all materials were annealed at 550 °C for 2 h.

The processing summarized above resulted in three classes of the "starting" materials for our detailed characterization and mechanical testing: CR, SR and SW. The textures and microstructures for each class of samples are shown in the Figs. 1 and 2a, respectively. Each material exhibits equiaxed, twin-free grains with an average grain size of about 15 μm. Note that each processing route induces orthotropic textures and, as a consequence, only one-quarter of the pole figures is shown. At first glance, the three classes of uranium exhibit similar textures with some subtle differences that have a large impact on mechanical properties. Each class exhibits strong (0 0 1) intensity in the through-thickness (TT3) direction, strong (0 1 0) intensity in the in-plane 1 (IP1) direction and strong (1 0 0) intensity in the in-plane 2 (IP2) direction. A primary difference is in the degree of in-plane (directions perpendicular to 3) isotropy with CR having the most in-plane isotropy and SW having the least. A good comparison is the (0 1 0) intensity in the IP1 and IP2 directions for each class where SW has

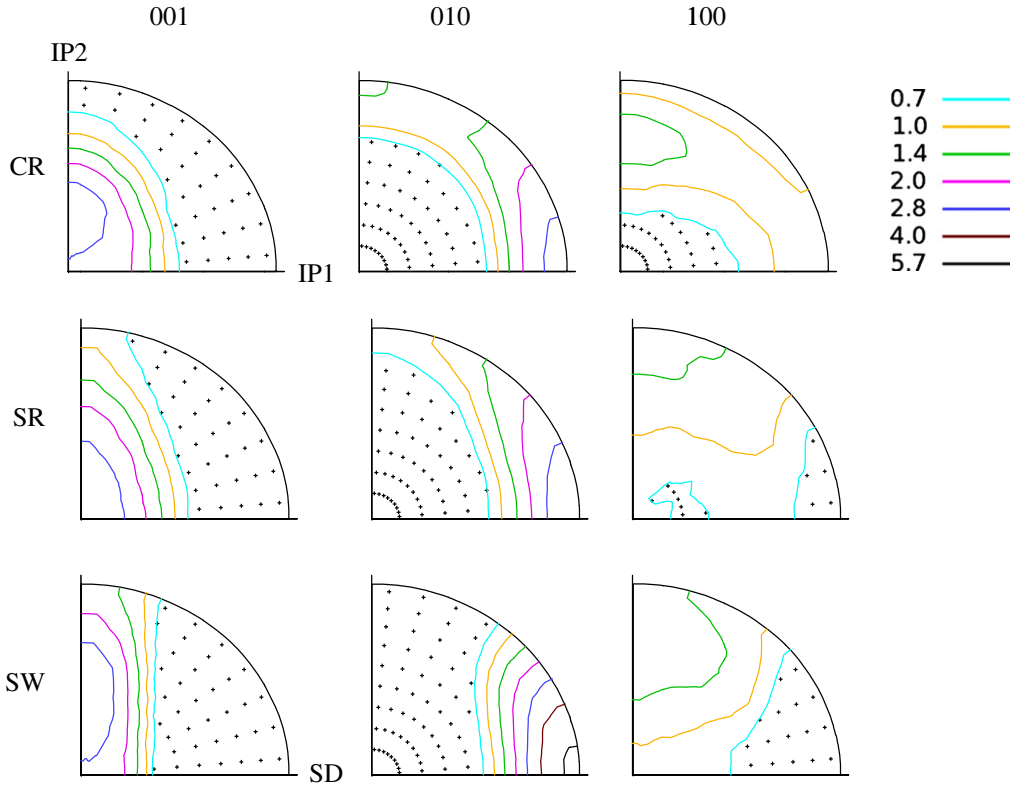

Fig. 1. Pole figures showing the initial texture in the as-annealed samples for each class of the material.

the biggest difference in (0 1 0) intensities in these directions and CR has the smallest difference.

For the rolled materials, tensile samples were machined in the IP1 and IP2 directions and compression samples were machined in the IP1, IP2 and TT directions where IP1 is the direction parallel to the final rolling direction and IP2 is the direction transverse to the final rolling direction. For the SW material, tensile and compression samples were machined from the SD(1) direction. The CR tensile samples had a flat dog-bone geometry with gage length cross-section dimensions of 2.5 mm × 6 mm and the SR and SW tensile samples had a round geometry with a gage diameter of 3 mm. All compression samples were right circular cylinders, some with 5 mm and some with 6.35 mm diameters. The samples are grouped and presented according to the macroscopic deformation mode to be imposed using the following conventions: IPC1, IPC2, IPT1, IPT2 and TTC3.

Constant-velocity tension and compression tests were performed at a nominal strain rate of $10^{-3}\,s^{-1}$ at room temperature using a screw-driven Instron. Polished tungsten carbide platens were used to load the compression samples lubricated with molybdenum disulfide grease to reduce frictional effects. The raw data was collected in the form of load and displacement, and was corrected for machine compliance before computing the true stress–true strain curves. Separate samples were deformed to true strains of 0.05, 0.1, 0.15, and 0.2 in compression and to true strains of 0.05, 0.1, 0.15, 0.2 and failure in tension.

The specimens were prepared for EBSD using the procedure reported in detail in Refs. [2,18]. The complete list of the samples examined by EBSD is shown in Table 1. Note that some of the microstructure and texture measurements are discussed in the paper, while more can be found in the supplementary material. The automated EBSD data collection was performed using a TSL camera attached to a FEI XL30 environmental scanning electron microscope at a voltage of 25 kV. The EBSD scans used to obtain representative texture information were run with 5–10 μm step sizes over an area of several square millimeters while the detailed microstructure scans were run with a 0.2 μm step size over an area of 200 μm × 100 μm.

3. Polycrystalline modeling

A mean-field, self-consistent method is used to model the mechanical behavior of the polycrystalline α-uranium. In the self-consistent approach, a polycrystal is represented with a set of grains (each having an orientation and a volume fraction) representative of the texture of the material. Each grain is treated as a viscoplastic inclusion embedded in a homogeneous effective medium, and the elementary inclusion problem is solved using a Green function approach [19,20]. Enforcing the macrohomogeneity condition of self-consistency between macroscopic stress and grain averages allows one to derive the viscoplastic properties of the effective medium. A detailed description of this viscoplastic self-consistent (VPSC) model can be found in

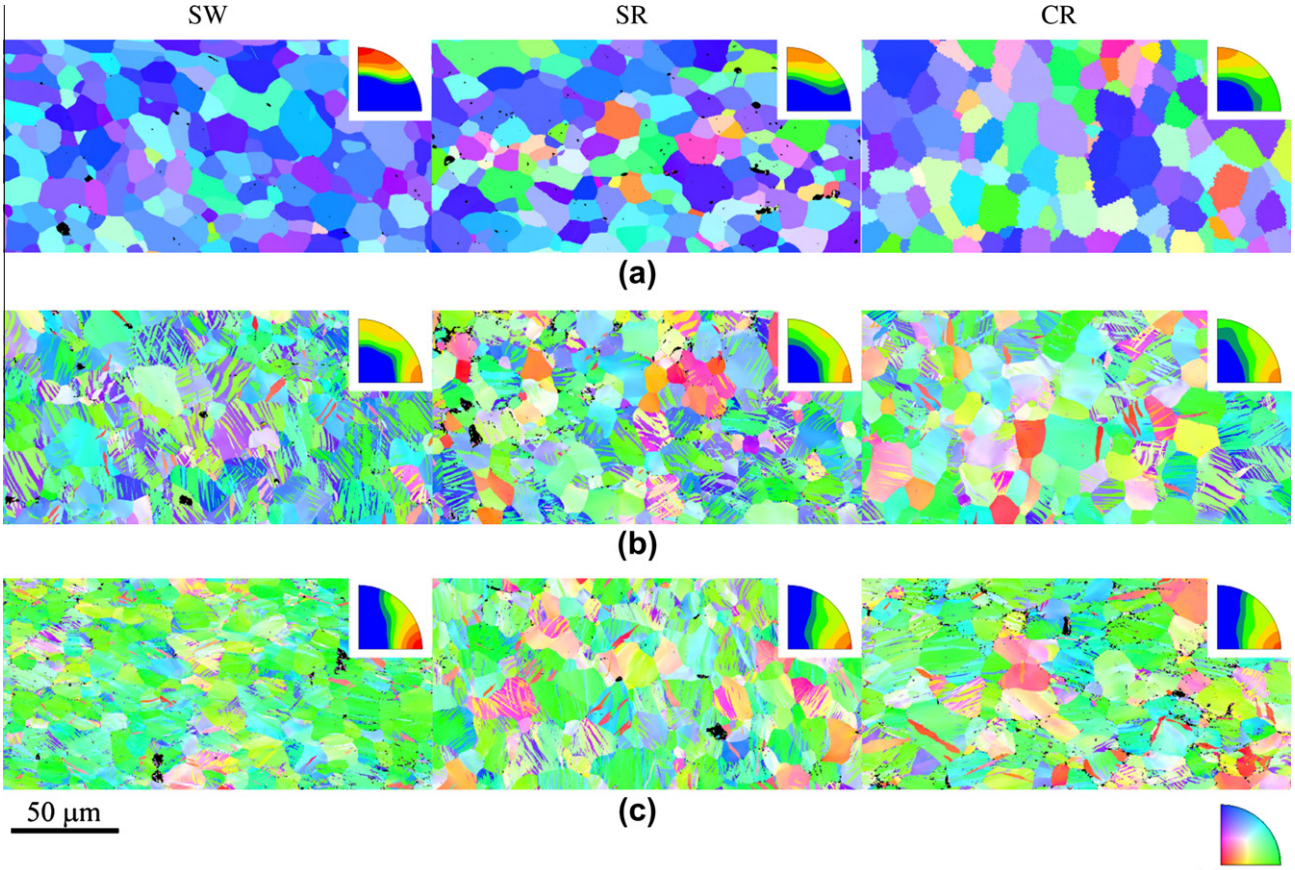

Fig. 2. Orientation maps of the microstructures for IPC1 to (a) 0.0, (b) 0.1 and (c) 0.2 strain. The colors in the orientation maps indicate the orientation of the compression axis with respect to the crystal reference frame. In the corner of each orientation map is the compression direction inverse pole figure showing the distribution of grain orientations in the compression direction. All IPF triangles have the crystal reference frame defined as [1 0 0] to the right, [0 1 0] upward and [0 0 1] in the center.

Table 1
List of characterized samples by EBSD as a function of strain.

		0.5	0.1	0.15	0.2
IPC1	CR		✓		✓
	SR				✓
	SW	✓	✓	✓	✓
IPC2	CR	✓	✓	✓	✓
	SR				✓
IPT1	CR	✓	✓	✓	✓
	SR		✓		✓
	SW				
IPT2	CR	✓	✓	✓	✓
	SR			✓	✓
TTC3	CR		✓		✓
	SR				✓

Ref. [20]. Here we concentrate on the equations necessary for our interpretations.

3.1. Hardening model

The equations underlying the single-crystal dislocation-based hardening law implemented within the VPSC homogenization framework are presented in Refs. [2,17] and are briefly summarized here. The modeling strategy includes a composite grain (CG) model for dealing with twinning reorientation and with the twinned domains [14]. In this work we critically test and calibrate the model using a comprehensive set of experimental data and provide new insights on the complex interactions between the deformation modes.

Plastic deformation in each grain occurs via the activation of both slip and twin modes. The corresponding slip or twin shear strain rate, $\dot{\gamma}^s$, on a given system, s, is quantified using the power-law relation:

$$\dot{\gamma}^s = \dot{\gamma}_0 \left| \frac{\tau^s}{\tau_c^s} \right|^{\frac{1}{m}} sign(\tau^s). \quad (1)$$

Here $\dot{\gamma}_0$, m, τ^s and τ_c^s, are the reference slip rate, rate sensitivity parameter, resolved shear stress and threshold stress on the slip system, respectively. It is noted that twin propagation is treated as a pseudo-slip mechanism, as originally proposed in Ref. [21]. A rationale for such modeling of twinning using the idea that twin thickening occurs primarily via the motion of twinning partial dislocations on the twinning plane was provided in Ref. [22].

Consistent with experimental evidence, the following four slip modes $(0\,1\,0)[1\,0\,0]$, $(0\,0\,1)[1\,0\,0]$, $1/2\{1\,1\,0\}\langle 1\,\bar{1}\,0\rangle$ and $1/2\{0\,2\,1\}\langle 1\,\bar{1}\,2\rangle$, and two twin modes $\{1\,3\,0\}\langle 3\,\bar{1}\,0\rangle$ and $\{1\,7\,2\}\langle 3\,\bar{1}\,2\rangle$ are considered as potential systems for accommodating the imposed plastic strain. Note here that the reciprocal of the $\{1\,7\,2\}\langle 3\,\bar{1}\,2\rangle$ twin mode, i.e. $\{1\,1\,2\}\langle 3\,\bar{7}\,2\rangle$, is not considered due to the fact that the activation of both mechanisms occurs under nearly identical loading conditions, making mathematical treatment of both mechanisms not practical. As discussed in Ref. [23], the atomic shuffles engendered by a type II twin and its reciprocal twin are different. Thus it is likely that the stress required to propagate each twin mode are different. The choice is made here to consider only the $\{1\,7\,2\}\langle 3\,\bar{1}\,2\rangle$ as it requires less shuffling than its reciprocal twin and it is usually observed in higher volume fractions.

The rate sensitivity parameter, m, is the same for both slip and twinning and taken to be $m = 0.05$. The reference slip rate, $\dot{\gamma}_0$, is set equal to the macroscopic strain rate so as to eliminate the rate sensitivity represented by m [24] to guarantee that shear will take place when the resolved shear stress is close to the threshold stress, τ_c^s. Rate and temperature effects are accounted for in the functional dependence of τ_c^s with rate and temperature. The critical resolved shear stresses (CRSS) of all slip systems or twin variants within one mode α (or family) in a grain are assumed to exhibit the same slip resistance.

In the case of slip, the CRSS is expressed as a sum of a friction stress, τ_0^α, a forest dislocation interaction stress, τ_{for}^α, and a dislocation substructure interaction stress, τ_{sub}^α, i.e.

$$\tau_c^\alpha = \tau_0^\alpha + \tau_{for}^\alpha + \tau_{sub}^\alpha. \tag{2}$$

The evolution of τ_{for}^α and τ_{sub}^α is governed by the evolution of the forest ρ_{for}^α and substructure ρ_{sub} dislocation densities, as described below. The effect of forest dislocation density is given by a traditional Taylor law [25]:

$$\tau_{for}^\alpha = \chi b^\alpha \mu^\alpha \sqrt{\rho_{for}^\alpha}, \tag{3}$$

where $\chi = 0.9$ is a dislocation interaction parameter. Dislocation dynamics simulations show that the contribution to hardening by dislocations stored within substructures, such as cell walls, can be accounted for using [26]:

$$\tau_{sub}^\alpha = k_{sub} b^\alpha \mu^\alpha \sqrt{\rho_{sub}} \log\left(\frac{1}{b^\alpha \sqrt{\rho_{sub}}}\right). \tag{4}$$

Here $k_{sub} = 0.086$ is an empirical parameter that recovers the Taylor law for low substructure dislocation densities [26]. Note that Eq. (4) takes into account the latent hardening effects between slip systems implicitly through the substructure dislocations arising from the effects of imperfect recovery on all slip systems within the grain, rather than by including those dislocations in Eq. (3).

The evolution of the stored forest density, ρ_{for}^α, is governed by competition between the rate of storage and the rate of dynamic recovery:

$$\frac{\partial \rho_{for}^\alpha}{\partial \gamma^\alpha} = \frac{\partial \rho_{gen,for}^\alpha}{\partial \gamma^\alpha} - \frac{\partial \rho_{rem,for}^\alpha}{\partial \gamma^\alpha} = k_1^\alpha \sqrt{\rho_{for}^\alpha} - k_2^\alpha \rho_{for}^\alpha, \tag{5}$$

where k_1^α is a rate-insensitive coefficient for dislocation storage by statistical trapping of gliding dislocations by forest obstacles and k_2^α is a rate-sensitive coefficient that accounts for dynamic recovery by thermally activated mechanisms. The latter coefficient, k_2^α, is given by [17]:

$$\frac{k_2^\alpha}{k_1^\alpha} = \frac{\chi b^\alpha}{g^a}\left(1 - \frac{kT}{D^\alpha b^3} ln\left(\frac{\dot{\varepsilon}}{\dot{\varepsilon}_0}\right)\right). \tag{6}$$

In Eq. (6), k, $\dot{\varepsilon}_0$, g^α and D^α are, respectively, the Boltzmann constant, a reference strain rate, an effective activation enthalpy and a drag stress. Dynamic recovery is often associated with thermal activation of dislocation cross-slip and climb, and the formation of dislocation substructures is concomitant with these recovery processes. As a consequence, in the model the rate of substructure development is coupled to the rate of recovery of all active dislocations through:

$$d\rho_{sub} = q \sum_\alpha f^\alpha b^\alpha \sqrt{\rho_{sub}} \frac{\partial \rho_{rem,for}^\alpha}{\partial \gamma^\alpha} d\gamma^\alpha, \tag{7}$$

where the product of q as a rate coefficient and f^α as an α-type dislocation recovery rate coefficient defines the fraction of dislocations that leads to substructure formation; the rest leads to annihilation.

The CRSS for twin activation accounts for a temperature-independent friction term, τ_0^β, and a latent hardening term coupling slip and twin systems. Therefore, the CRSS for twinning is given by:

$$\tau_c^\beta = \tau_0^\beta + \mu^\beta \sum_\beta C^{\alpha\beta} b^\beta b^\alpha \rho_{for}^\alpha. \tag{8}$$

Here μ^β, b^β, and $C^{\alpha\beta}$ are the elastic shear modulus on the system, the Burgers vector or shear direction of a given system, and the latent hardening matrix, respectively. The twin transformation is modeled via the CG model [14]. In brief, CG consists of identifying in each grain the twin system with the highest shear-rate among all active twin systems, i.e. the predominant twin system (PTS) in each grain, and partitioning the grain into a stack of flat ellipsoids having the crystallographic orientation of the predominant twin and the matrix, respectively. The short axis of the ellipsoids is perpendicular to the twin plane. As more shear is contributed by the twin, volume fraction is transferred from the parent to the twin: the ellipsoids representing the twins thicken, and the ones representing the parent shrink. Except for the volume transfer coupling, the twin and the parent ellipsoids are treated as independent inclusions in the model.

3.2. Simulation set-up and yield stress

The discrete distributions of orientations used in the simulations are constructed from the EBSD measurements done on the annealed samples of each type of material, i.e.

CR, SR and SW. The measured EBSD sections comprise of well over 100,000 grains, and are reduced to 10,000 orientations chosen so as to reproduce the experimental textures shown in Fig 1. The pole figures of the simulation textures are essentially indistinguishable from the experimental ones depicted in Fig. 1, and are not shown. Axial tension or compression up to 20% strain is simulated by imposing 0.2% strain increments along the corresponding direction, while enforcing zero average stress along the two lateral directions of the sample. The hardening parameters are calibrated using the experimental data presented in the previous section. They are given in Tables 2 and 3 for the slip modes and the twin modes, respectively, and will be discussed in the subsequent sections.

The mechanical properties of α-uranium are characterized by strong thermal, elastic and plastic anisotropies. As a consequence, temperature changes during processing result in unavoidable internal stresses in uranium aggregates. In addition, large differences in CRSS between different modes are typical. These effects lead to an extended elastoplastic transition upon loading. The objective of the present study is to understand the plastic deformation mechanisms and their interactions via the use of the dislocation density constitutive model described above. However, because the viscoplastic formulation does not capture the elastoplastic transition, calibrating the hardening law parameters with VPSC from the beginning of deformation leads to values not representative of the purely plastic process. As a consequence, we devised a procedure for estimating the strain associated with the end of the elastoplastic transition, and so for defining a yield point. The comparison between VPSC and experimental results is done starting at the strain at yield.

The procedure is based on first running an elastoplastic self-consistent (EPSC) simulation based on the model originally proposed by Turner and Tomé [27], and adapted recently by Clausen et al. [28] to include the dislocation-based hardening law described above. We simulate cooling from the stress-free state at 400 °C [9] to room temperature to build-up the annealed-state internal stresses followed by a 3% tensile or compressive loading along each of the main sample axes. This simulation is approximate because it disregards plastic deformation during cooling, assumes no twinning activity during the elastoplastic transition, and uses hardening parameters which are close to but not equal to those eventually fit using VPSC. The determination of the yield stresses is rather ambiguous. One extreme is to consider the initiation of elastoplasticity when slip starts in a few grains but deformation is still mostly controlled by elasticity. The other extreme is when every grain in the material has reached full plasticity. Because of the extended character of the elastoplastic transition, both states are considerably apart, and in the present study we use a criterion based on an average measure of plastic activity. Specifically, we compute the average number of active systems (AVACS) per grain, in EPSC and VPSC simulations, as a function of strain (in VPSC a system is considered active if the shear rate it contributes is at least 5% of the shear rate of the most active system in the grain). We define the yield stress where the monotonically increasing AVACS predicted by EPSC as the elastoplastic transition takes place equals the AVACS predicted by VPSC in the first loading step. The strains used to shift the VPSC curves and the corresponding yield stresses are summarized in Table 4 for each of the materials and tests.

Table 3
Twin mode hardening parameters.

	$\beta = 1\{130\}$	$\beta = 2\{172\}$
τ_o^α (MPa)	70	235
$C^{\alpha\beta}$, $\alpha = 1$	1000	1000
$C^{\alpha\beta}$, $\alpha = 2$	500	500
$C^{\alpha\beta}$, $\alpha = 3$	500	500
$C^{\alpha\beta}$, $a = 4$	3100	1000
b^β (nm)	0.1036	1.433

While twinning contribution to shear is not considered in the EPSC simulation, it is implicitly assumed that during the elastoplastic transition there will be some twin nucleation induced by the slip activity. This is important since our VPSC simulations allow twinning to start right from the beginning of the deformation, and current theories [16,29,30] for the activation of deformation twinning rely on previous dislocation activity and stress concentrations at boundaries resulting from prior deformation.

4. Results

Fig. 4 compares the measured and predicted stress–strain responses for the three classes of α-uranium

Table 2
Slip mode hardening parameters.

	$\alpha = 1$ [100](010)	$\alpha = 2$ [100](001)	$\alpha = 3$ $\langle 1\bar{1}1\rangle\{110\}$	$\alpha = 4$ $\langle 1\bar{1}2\rangle\{021\}$
b^α (nm)	2.85×10^{-1}	2.85×10^{-1}	6.51×10^{-1}	11.85×10^{-1}
κ_1^α (m^{-1})	1.65×10^9	9.0×10^8	3.3×10^8	1.5×10^8
$\dot{\varepsilon}_0^\alpha$ (s^{-1})	10^7	10^7	10^7	10^7
g^α	3.2×10^{-4}	3.2×10^{-4}	1.0×10^{-3}	4.0×10^{-3}
D_o^α (MPa)	4100	3000	700	1000
f^α	20	0	20	0
τ_o^α (MPa)	188	375	500	600
q	4	4	4	4

Table 4
Yield stress (MPa) corresponding to the 0.002 off-set strain and to the estimated strain using EPSC at the onset of VPSC calculations. Values of yield stress at the onset of VPSC calculations are given for the experimental curves as well as for the simulated curves.

	CR			SR			SW		
Strain Yield stress	Offset Exp.	EPSC estimate Exp.	EPSC estimate Sim.	Offset Exp.	EPSC estimate Exp.	EPSC estimate Sim.	Offset Exp.	EPSC estimate Exp.	EPSC estimate Sim.
IPC1	0.002 300	0.016 460	0.016 455	0.002 290	0.014 405	0.014 405	0.002 280	0.010 320	0.010 320
IPC2	0.002 335	0.017 510	0.017 585	0.002 495	0.014 650	0.014 650			
IPT1	0.002 280	0.025 605	0.025 615	0.002 420	0.018 660	0.018 660	0.002 500	0.021 740	0.021 740
IPT2	0.002 305	0.023 520	0.023 520	0.002 320	0.020 485	0.020 485			
TTC3	0.002 560	0.021 770	0.021 805	0.002 590	0.022 805	0.022 805			

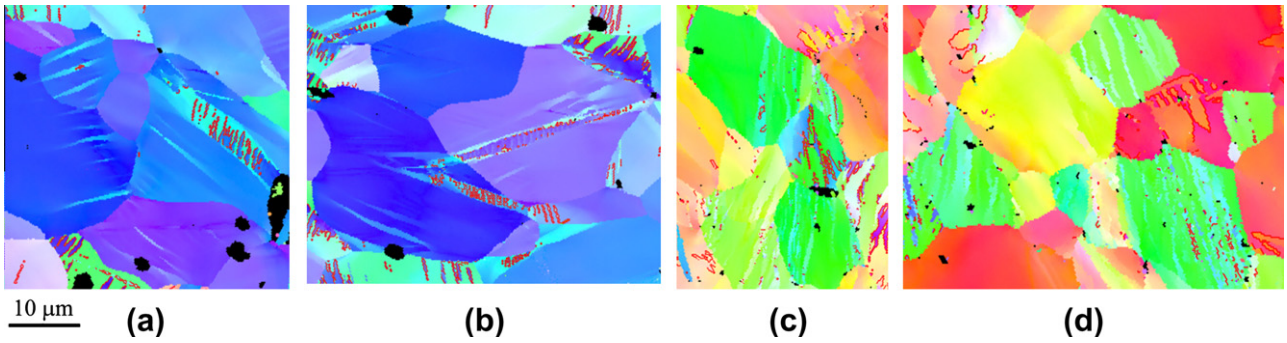

Fig. 3. Orientation maps for SR material deformed by IPT1 0.1 strain (a and b) and by IPC2 0.2 strain (c and d). The colors in the orientation maps indicate the orientation of the tension/compression axis with respect to the crystal reference frame. {1 3 0} twin boundaries are colored red. Regions that appear similar to twins but do not have red boundaries are the deformation bands discussed in the text.

samples measured in compression and tension in the three mutually perpendicular directions described earlier. The stress–strain responses confirm the strong anisotropy exhibited by α-uranium in its plastic response within each of the sample classes. Between the sample classes, the strongest textured SW sample exhibits the highest degree of anisotropy. Table 4 displays the strain-at-yield calculated with the criterion explained above, together with the experimental and VPSC predicted yield stress at that strain for all cases. Observe that the strain-at-yield always exceeds 1% and can be as high as 2.5% (CR-IPT1). For completeness, and also to show how using a classic criterion can give very different results, we show in Table 4 the yield stress associated with the 0.002 offset yield-strength criterion. The hardening parameters calibrated in this paper successfully reproduce the measured mechanical response of the IPC1, IPT2 and TTC3 loading test and reasonably well reproduce those corresponding to the IPC2 and IPT1 loading directions. Since the only difference between materials is the texture, the implication is that the hardening parameters are qualitatively right. In addition, in all cases the model captures the characteristic increase in hardening rate associated with twinning activity, which manifests as an inflection in the stress–strain response. The implication is that the twining model is qualitatively correct. It was found that the constants established in the previous work [2] did not reproduce well some of the measured stress–strain curves and texture evolution in the samples with higher degrees of texture anisotropy. Therefore, the new hardening constants differ from those reported in the previous paper [2] in which only the CR mechanical response and texture evolutions were available.

The EBSD maps of the IPC1 and IPT1 deformed samples at strains of 0.1 and 0.2 are shown in Figs. 2 and 3. Fig. 5 shows the comparison between the measured and predicted textures at a strain of 0.2. Visually the model captures well the texture evolution in all CR, SR and SW loading conditions. The supplementary file contains comparisons for all textures measured at strains of 0.05, 0.1 and 0.15 as reported in Table 1.

The difference between the predicted and the measure textures are quantified using the pole figure difference (PFD) parameter. The PFD factor is defined as:

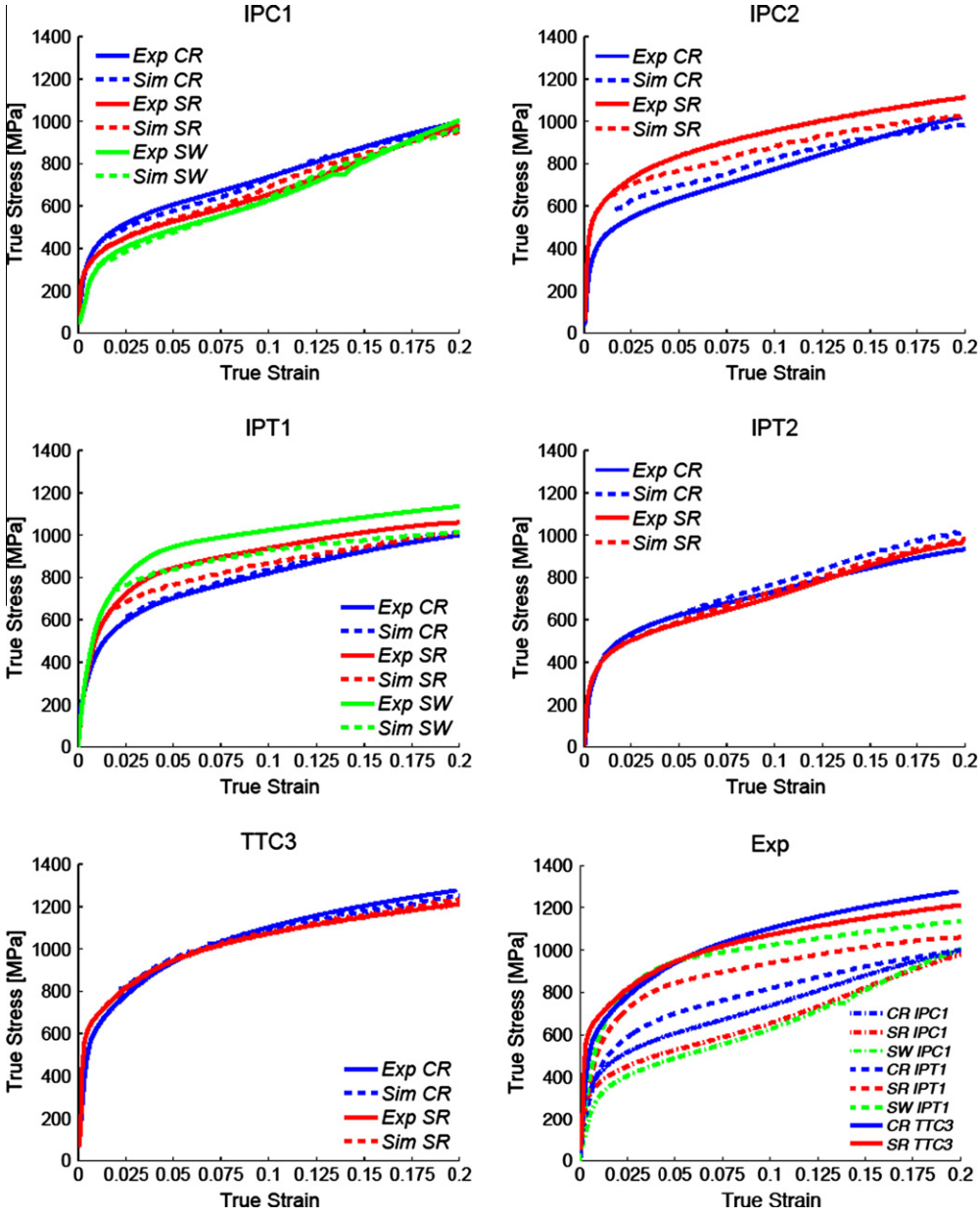

Fig. 4. Simple compression and simple tension response at room temperature on annealed samples of clock-rolled (CR), straight-rolled (SR) and swaged (SW) uranium along the direction indicated in the plots: measured (solid lines) and predicted (dashed lines) true stress–true strain response. The last plot is a collection of experimental stress–strain curves showing the variation of properties obtained from different starting textures.

$$PFD^{hkl} = \frac{\int_{\varphi=0}^{2\pi}\int_{\theta=0}^{2\pi}\left|I^{meas}_{(\varphi,\theta)} - I^{pred}_{(\varphi,\theta)}\right| sin\theta d\theta d\varphi}{\int_{\varphi=0}^{2\pi}\int_{\theta=0}^{2\pi}\left|I^{meas}_{(\varphi,\theta)} + I^{pred}_{(\varphi,\theta)}\right| sin\theta\, d\theta\, d\varphi}. \quad (9)$$

The average value of the PFD factor, taken over (001), (010) and (100) pole figures, is reported in Table 5. A value of PFD = 0 corresponds to a perfect match between the measured and the predicted pole figures and PFD = 1 corresponds to a perfect mismatch. Two textures with a PFD < 0.2 are considered to be in good agreement, and PFD < 0.1 represents excellent agreement. The computed values show that the present model and the hardening parameters established in this paper successfully capture concomitant texture evolution in the CR, SR and SW material.

An accurate prediction of the mechanical response and texture evolution of the 12 tested samples is an indication that the predicted relative activities of the slip and twin modes contributing to plastic deformation are reasonable. Two sets of relative activity plots of SR samples are shown in Fig. 6, with each set consisting of two plots: one for the mode activity within the parent material and one for the mode activity within the twinned material. Only the SR case is displayed because the activities for the CR and SW cases are qualitatively similar to SR for any given testing direction. The predicted and measured {130} evolution

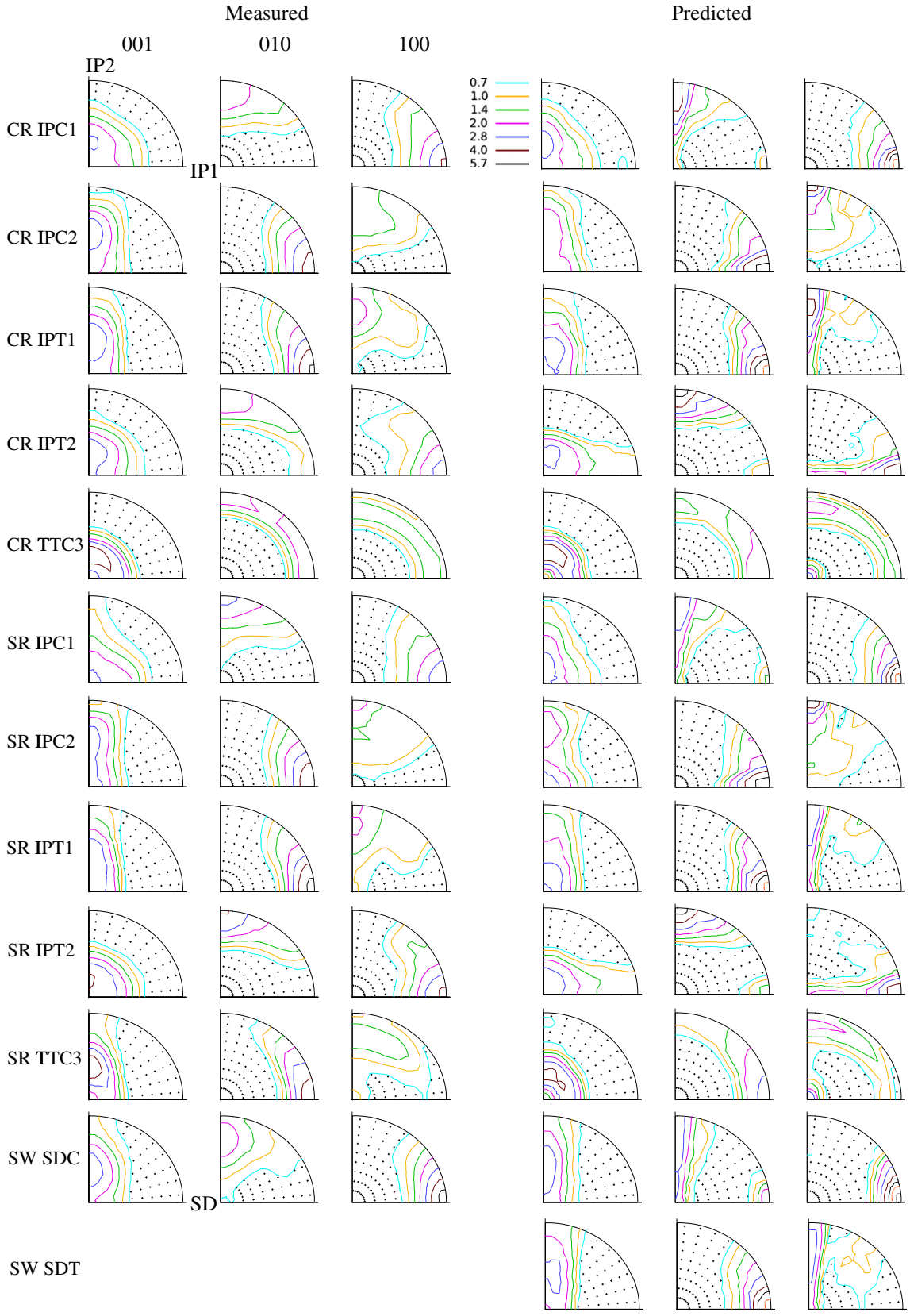

Fig. 5. Pole figures showing measured (on the left) and predicted (on the right) textures at the strain of 0.2 for the clock-rolled (CR), straight-rolled (SR) and swaged (SW) samples deformed along the directions indicated in the figure.

Table 5
Average pole figure difference (PFD) parameter between the measured (EBSD) and the predicted (VPSC) textures at the strain of 0.2.

	Initial	IPC1	IPC2	IPT1	IPT2	TTC3
CR	0.02636	0.14917	0.12421	0.14546	0.20719	0.12230
SR	0.02803	0.17235	0.14346	0.14144	0.18619	0.18310
SW	0.03983	0.200173	–	–	–	–

of twin volume fractions are shown in Fig. 7 for all samples and testing directions.

Considering that the CG model represents a simplified scheme for treating twinning (it only tracks the PTS in any given grain), and considering that the experimental twin fraction measurements slightly underestimate the actual twin fractions [2], we regard the match between experimental and simulated twin fractions in Fig. 7 as very good.

5. Discussion

5.1. Deformation regime dominated by profuse twinning and secondary slip

A simple Schmid factor analysis of the pole figures for the annealed samples in Fig. 1 suggests that the fraction of grains favorably oriented for twinning increases from the CR to the SW samples when loaded in IPC1 and IPT2. Fig. 8 shows the area fraction distribution of variant 1 {1 3 0} twin Schmid factors for IPC1 loading in each of the materials both before and after deformation to a strain of 0.2. The substantial change that the distribution experiences with deformation is almost entirely due to twin activity.

The concave shape of the IPC1 and IPT2 true stress–true strain curves shown in Fig. 4 is also an indication of twinning-dominated deformation. The associated strain-hardening behaviors shown in Fig. 9 confirm the major contribution of twinning to plasticity of α-uranium deformed in the IPC1 and IPT2 directions. The strain-hardening rates plotted in Fig. 9 are computed numerically from the stress–strain curves shown in Fig. 4 and are normalized by the shear modulus to facilitate comparisons with published data on other metals [16]. It is seen that the hardening rates reach a minimum prior to increasing to a local maximum and eventually decrease. The plots of strain-hardening rate also show that the twinning activity increases from the CR material to the SW material deformed in IPC1.

It is evident from this combined experimental and modeling study that twinning plays a significant role in the IPC1 and the IPT2 deformation of α-uranium at room temperature. The volume fraction of twinned material in the SW IPC1 is more than 70% at a strain of 0.2. It is higher than in the CR and the SR samples, which show twin volume fractions of about 40% and 55%, respectively. The EBSD measurements show the fraction of {1 3 0} twins to be far greater than that of {1 7 2} twins. By a strain of 0.2, EBSD orientation maps show deformation twins that often encompass entire grains. The respective twin resistances for {1 3 0} and {1 7 2} twins are predicted to be 88 and 235 MPa, respectively (Table 3). Compared with the slip mode resistances (Table 2), the {1 3 0} twin mode is the easiest deformation mode.

Deformation twins, while growing and accommodating plastic strain, reorient grains either to harder or to softer orientations, so inducing either texture hardening or softening. The activation of {1 3 0} twinning in uranium in both tension and compression and {1 7 2} twinning in compression results in texture hardening. The fact that all three IPC1 stress–strain curves exhibit larger slopes with SW being the largest is evidence that twinning induces hardening by reorientation (Fig. 9). Because twins in uranium are observed to grow rapidly, for modeling it is sufficient to account only for the texture hardening effect induced by twins while ignoring Hall–Petch-type effects. The fact that the model captures the highly anisotropic mechanical behavior of α-uranium quite well clearly confirms our reasoning. The model explicitly accounts for the texture hardening by reorienting the grains.

The predicted deformation modes show substantial activity of deformation twinning in the parent material. In order to further deform, the twinned volumes require activation of secondary slip involving the relatively hard $\{1\,1\,0\}\langle 1\,\bar{1}\,0\rangle$ mode (see IPC1, IPT2 in Fig. 6). The effect is more pronounced in the SW material than in the CR material deforming in the IPC1 and IPT2 directions.

5.2. Deformation regime dominated by slip-band formation

We focus here on the monotonic IPC2 and IPT1 loading. It is found that the model is less precise for these than for the previous cases. While twinning is present in these cases, it is predicted that (0 1 0)[1 0 0] slip contributes more significantly to plastic deformation with (0 0 1)[1 0 0] contributing to a lesser extent. The activity plots in Fig. 6 and the evolution of the strain-hardening rates as a function of normalized stress in Fig. 10 also show the presence of twinning as a deformation mechanism, but the increasing work-hardening rate commonly attributed to twinning is not as well defined as in the previous case. Twinning is accompanied by other potential hardening mechanisms: twin–slip interaction and secondary slip. It is found that the plateau reached is the consequence of both twinning and the fact that the most active deformation mode reaches stage 4 hardening. The SW IPT1 curve exhibits less hardening and less twin activity (note the hardening rates in Fig. 10).

Finally, EBSD observations show the presence of bands associated with a combination of $\{1\,1\,0\}\langle 1\,\bar{1}\,0\rangle$ and

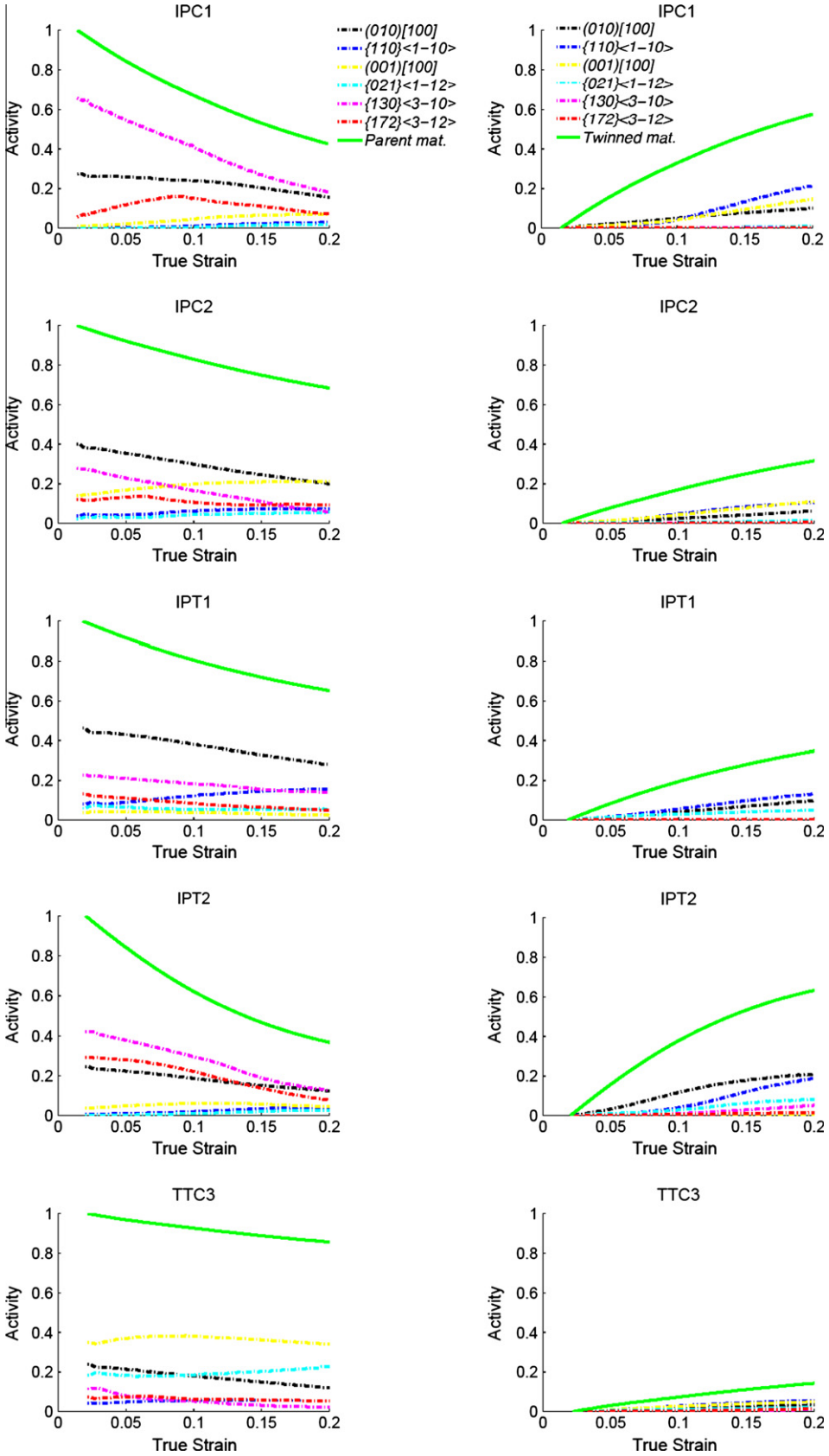

Fig. 6. Predicted relative activities of each deformation mode contributing to plasticity in both the parent grain (on the left) and the twin (on the right) for SR samples in the macroscopic deformation mode groups (IPC1, IPC2, IPT1, IPT2 and TTC3). Also plotted is the parent material (on the left) and twinned material (on the right) volume fraction.

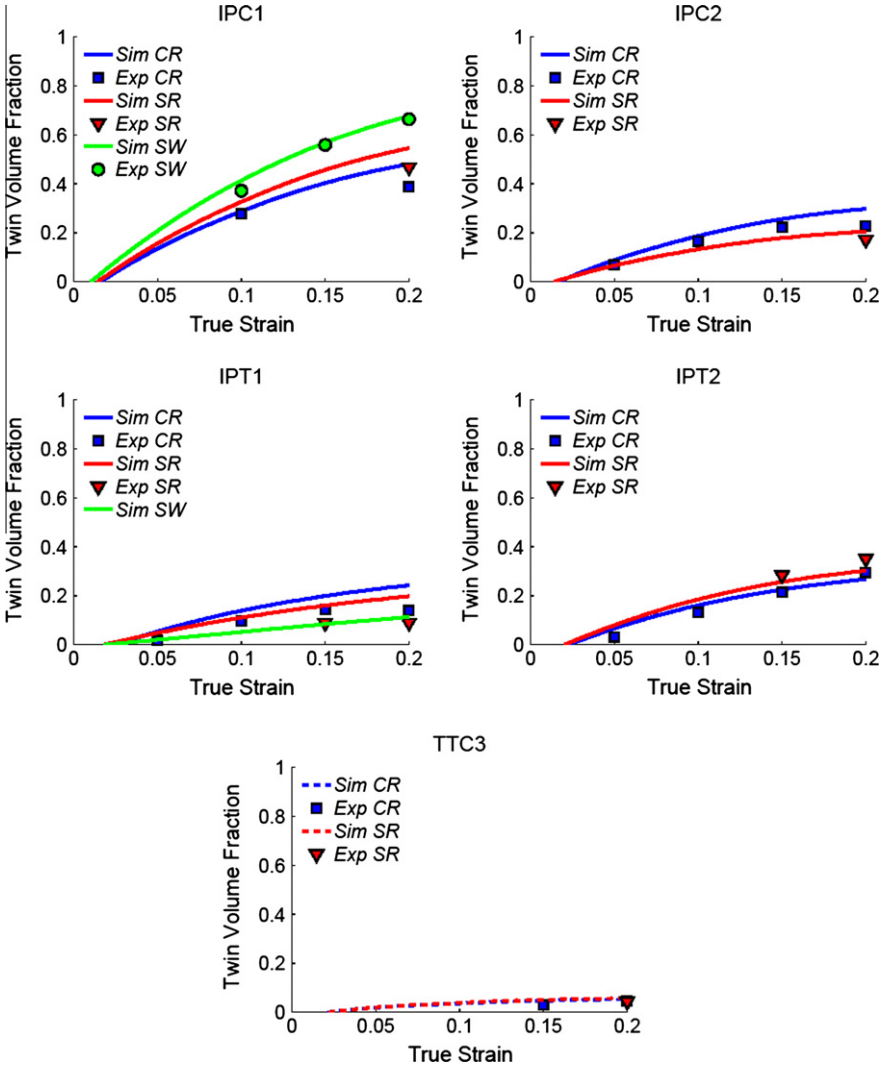

Fig. 7. Evolution of {130} twin volume fractions in the samples predicted by VPSC (lines) and measured by EBSD (symbols) as a function of strain.

(010)[100] slip in grains oriented near (010) tension and (100) compression. Although the EBSD data is not definitive because of its 2-D nature, the reorientation within the bands and the orientation of the band boundaries is consistent with these slip modes. Within the bands, we observe a rotation toward (010) in compression and toward [100] in tension, both rotations occurring about [001]. In addition, 2-D-based {110} plane traces consistently align with the band boundary traces. Interestingly, we observe {130} twins within these bands and terminating at the band boundaries. While the grains are initially poorly oriented for {130} twinning, the localized slip within the bands results in a new orientation that is favorable for twinning. To the best of our knowledge, this is the first observation of localized twinning occurring within localized slip bands. The non-zero value of the coefficient $f^{\alpha} = 20$ defining the fraction of α-type dislocation recovery rate leading to substructure formation in the model is consistent with this observation. The slip band effect is more pronounced for (100) compression than (010) tension, most likely because $\{110\}\langle 1\bar{1}0\rangle$ slip is the only mechanism that will accommodate (100) compression, whereas (010) tension is also accommodated by $\{021\}\langle 11\bar{2}\rangle$ slip.

5.3. Slip-dominated deformation regime

When the SR and the CR samples are subjected to TTC tests, it is observed and predicted that most of the imposed plastic deformation is accomodated by slip activity. After 0.2 strain, less than 20% of the grains were reoriented by twinning. In addition, it is found that little texture evolution occurs during deformation (see Fig. 5).

It is predicted that the (001)[100], (010)[100] and $\{021\}\langle 1\bar{1}2\rangle$ slip modes contribute to the plastic deformation with a smaller contribution of $(1\bar{1}0)[110]$ slip. Activation of all slip modes can be rationalized by the low number of glide systems per mode available in α-uranium. The two dominant mechanisms activated are (010)[100] and $(021)\langle 1\text{–}12\rangle$ slip. The (001)[100] slip mode has an initial resistance of 188 MPa while the $\{021\}\langle 1\bar{1}2\rangle$ has a

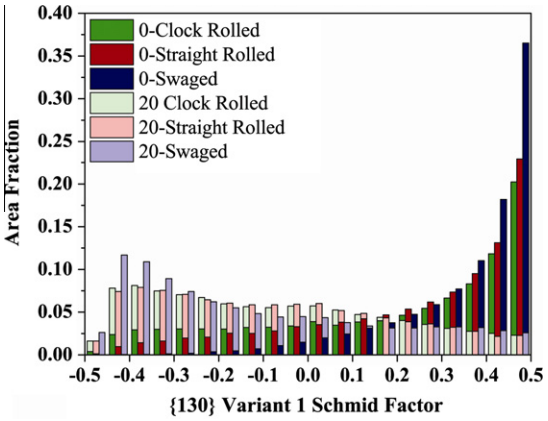

Fig. 8. Area fraction distribution of variant 1 Schmid factor before deformation and after IPC1 deformation for CR, SR and SW samples. Note the shift in the distribution with deformation for all three classes of the samples.

resistance of 600 MPa. It is expected here that substantial cross-slip could occur as both the (001)[100] and (010)[100] systems are active simultaneously and they are predicted to have the same activation enthalpy g^{α}. As both the (001)[100] and the (010)[100] dislocations have the same Burgers vector and do not lead to the same amount of debris formation, it is concluded that the structure of the dislocation cores are likely to be different.

Interestingly, the parameters obtained suggest that only (010)[100] and $\{1\bar{1}0\}\langle 110\rangle$ slip are likely to induce stage 4 (i.e. the values of f are not null). However, the contribution of the former is clearly dominant. Therefore, the interaction between the (010)[100] dislocations with all other active modes is the primary sources of debris, possibly in the form of the sessile or immobilized dislocation segments. Finally, the large empirical value of the latent hardening constant that we fit by coupling $\{021\}\langle 1\bar{1}2\rangle$ and {130} twins ($C^{41} = 3100$) suggests that this slip activity is delaying the twin nucleation.

6. Conclusions

The following primary conclusions are drawn from this study:

(a) Wrought uranium with three different "initial" textures was created by different combinations of thermomechanical processes. The initial crystallographic texture is a significant factor in determining the level of anisotropy in the mechanical behavior of α-uranium. As an example, the samples deformed in the

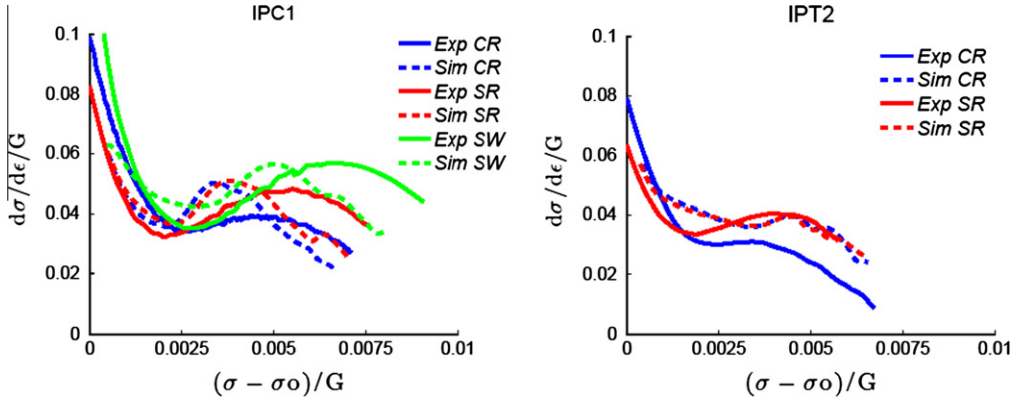

Fig. 9. Normalized strain-hardening rates corresponding to the true stress–true strain curves in Fig. 2 for IPC1 and the IPT2 deformation.

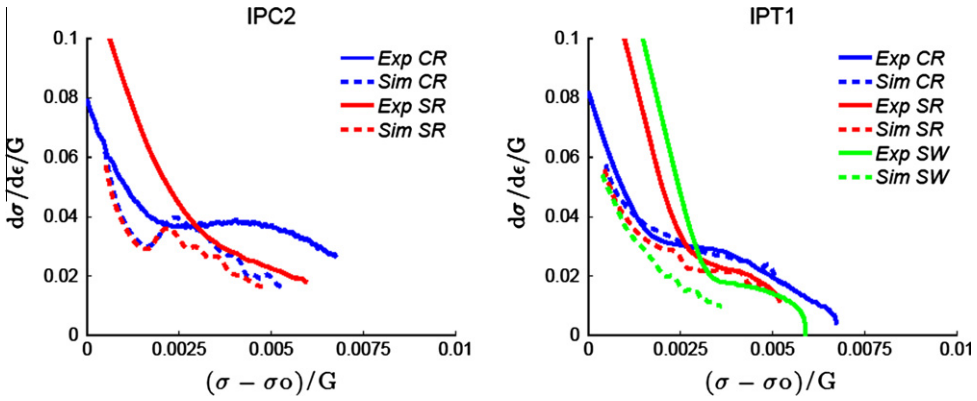

Fig. 10. Normalized strain-hardening rates corresponding to the true stress–true strain curves in Fig. 2 for IPC2 and IPT1 deformation.

IPT1 direction have a yield stress of 280 MPa for the CR material and 500 MPa for the SW material, respectively.

(b) Among the samples studied, a majority of grains are favorably oriented for {1 3 0} twinning in the SW samples, and when deformed in the IPC1 direction, the volume fraction of twinned material is greater than 70% at a strain of 0.2. The SR and the CR samples also exhibited profuse {1 3 0} twinning for IPC1. IPT2 deformation was similar to IPC1 deformation. The {1 3 0} twins contribute to the hardening of the material mainly by reorienting the grains from a softer to a harder orientation.

(c) The samples deformed in IPC2 and IPT1 exhibit a smaller twinning contribution and larger slip contribution to plasticity. In addition, activity of $\{1\,1\,0\}\langle 1\bar{1}\,0\rangle$ and (0 1 0)[1 0 0) type dislocations form localized slip bands. The combined activity of these modes within the bands results in crystallographic rotations from unfavorable to more favorable orientations for twinning, and {1 3 0} twins are found within the bands in these samples.

(d) Slip-dominated deformation was observed in SR and the CR samples subjected to TTC deformation. It is found here that little texture evolution occurs during deformation.

(e) The hardening law adapted from the earlier studies on hexagonal metals and implemented within the VPSC homogenization scheme performs well in capturing the anisotropic strain hardening and the texture evolution in all 12 studied samples. The predictions of the deformation mode activities are consistent with experimental observations. The good modeling results represent a significant incentive for incorporating the present VPSC-based constitutive model of uranium into finite-element frameworks [31,32] to facilitate process design and mechanical evaluation of uranium components.

Acknowledgements

This work was performed under Contract Number DE-AC52-06NA25396 with the US Department of Energy. The EBSD work was performed in the electron microscopy laboratory (EML) at Los Alamos. The authors wish acknowledge Duncan Hammon for rolling, heat treating and swaging the material, Tim Beard for machining the mechanical test specimens, Mike Lopez and Carl Cady performing some of the mechanical tests, and Ann Kelly for metallographic assistance.

Appendix A. Supplementary material

Supplementary data associated with this article can be found, in the online version, at doi:10.1016/j.actamat.2011.10.041.

References

[1] Cahn RW. Acta Metall 1953;1:49.
[2] McCabe RJ, Capolungo L, Marshall PE, Cady CM, Tomé CN. Acta Mater 2010;58:5447.
[3] Cahn R. Acta Crystall 1951;4:470.
[4] Anderson RG, Bishop JW. The effect of neutron irradiation and thermal cycling on permanent deformations in uranium under load. In: Symposium on Uranium and Graphite. London: The Institute of Metals; 1962. p. 17.
[5] Daniel JS, Lesage B, Lacombe P. Acta Metall 1971;19:163.
[6] Fisher ES, McSkimin HJ. J Appl Phys 1958;29:1473.
[7] Lebensohn RA, Tomé CN. Mater Sci Eng A 1994;175:71.
[8] Rollett AD. Comparison of experimental and theoretical texture development in alpha-uranium. In: Lowe TC, Rollett AD, Follansbee PS, Daehn GS, editors. Symposium on modeling the deformation of crystalline solids, 361. Warrendale (PA): TMS; 1991. p. 361.
[9] Brown DW, Bourke MAM, Clausen B, Korzekwa DR, Korzekwa RC, McCabe RJ, et al. Mater Sci Eng A 2009;512:67.
[10] Choi CS, Staker M. J Mater Sci 1996;31:3397.
[11] Yoo MH. J Nucl Mater 1968;26:307.
[12] Basinski ZS, Szczerba MS, Niewczas M, Embury JD, Basinski SJ. Revue de Metallurgie. Cahiers D'Inform Tech 1997;94:1037.
[13] Asgari S, El-Danaf E, Kalidindi SR, Doherty RD. Metall Mater Trans A: Phys Metall Mater Sci 1997;28A:1781.
[14] Proust G, Tomé CN, Kaschner GC. Acta Mater 2007;55:2137.
[15] Proust G, Tomé CN, Jain A, Agnew SR. Int J Plast 2009;25:861.
[16] Knezevic M, Levinson A, Harris R, Mishra RK, Doherty RD, Kalidindi SR. Acta Mater 2010;58:6230.
[17] Beyerlein IJ, Tomé CN. Int J Plast 2008;24:867.
[18] McCabe RJ, Teter DF. J Microsc 2006;223:33.
[19] Lebensohn RA, Tomé CN. Acta Metall Mater 1993;41:2611.
[20] Lebensohn RA, Tome CN, Castaneda PP. Philos Mag 2007;87:4287.
[21] Van Houtte P. Acta Metall Mater 1978;26:591.
[22] Capolungo L, Beyerlein IJ, Tomé CN. Scripta Mater 2009;60:32.
[23] Crocker AG. J Nucl Mater 1965;16:306.
[24] Kok S, Beaudoin AJ, Tortorelli DA. Int J Plast 2002;18:715.
[25] Mecking H, Kocks UF. Acta Metall Mater 1981;29:1865.
[26] Madec R, Devincre B, Kubin LP. Phys Rev Lett 2002;89:255508.
[27] Turner PA, Tomé CN. Acta Metall Mater 1994;42:4143.
[28] Clausen B, Brown DW, Tomé CN, Balogh L, Vogel SC. Engineering related neutron diffraction measurements probing strains, texture and microstructure. In: Hansen N, Juul Jensen D, editors. Proceedings of the 31st Risø international symposium on materials science. "Challenges in materials science and possibilities in 3D and 4D characterization techniques. Risø: Risø National Laboratory; 2010. p. 11.
[29] Christian JW, Mahajan S. Prog Mater Sci 1995;39:1.
[30] Wang J, Beyerlein IJ, Tomé CN. Scripta Mater 2010;63:741.
[31] Segurado J, Lebensohn RA, Llorca J, Tomé CN. Int J Plast 2012;28:124.
[32] Knezevic M, McCabe RJ, Lebensohn RA, Tomé CN, Mihaila B., in preparation.